A New Four Point Circular-Invariant Corner-Cutting Subdivision for Curve Design

Jian-ao Lian
Prairie View A&M University

A New Four Point Circular-Invariant
Corner-Cutting Subdivision for Curve Design

Jian-ao Lian

Department of Mathematics
Prairie View A&M University
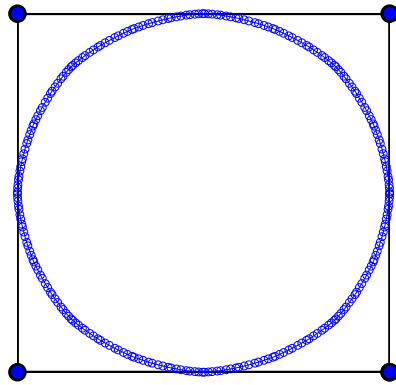Prairie View, TX 77446-0519 USA
JiLian@pvamu.edu

Abstract

A 4-point nonlinear corner-cutting subdivision scheme is established. It is induced from a special C-shaped biarc circular spline structure. The scheme is circular-invariant and can be effectively applied to 2-dimensional (2D) data sets that are locally convex. The scheme is also extended adaptively to non-convex data. Explicit examples are demonstrated.

Keywords: Biarc; Circular-Invariant; Computer-aided geometric design; Nonlinear; Subdivision

MSC 2010: 14H50; 17A42; 65D17; 68U07

1. Introduction

SUBDIVISION has been one of the most efficient ways for curve and surface design in computer graphics, with successful applications in computer animation (e.g., film production) and the video game industry in particular. Though linear subdivision schemes are desired and easy to implement in practice, nonlinear subdivision schemes can achieve some features that linear ones cannot. In this paper, a 4-point nonlinear subdivision scheme for 2D curve design is established. This scheme is said to be *circular-invariant* (Lian, et al. [18]), meaning a full circle will be generated for any initial regular planar polygon. It can be effectively applied to any 2D sets of data which are convex. Similar notions in the literature include *circular-preserving*

464

Applications and Applied Mathematics: An International Journal (AAM), Vol. 7 [2012], Iss. 1, Art. 30

AAM: Intern. J., Vol. 7, Issue 1 (June 2012)   465
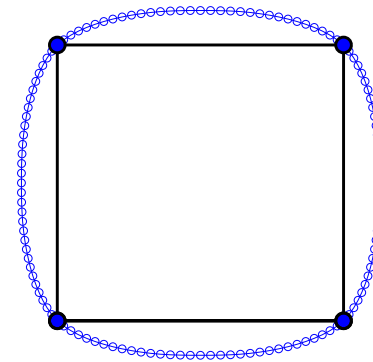
(a) de Rham-Chaikin

(b) DLG 4-point

(c) 4-point N_6-Binary
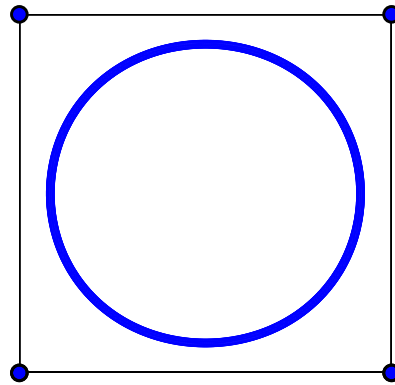
(d) 4-point N_5-Ternary

Fig. 1. An illustration for subdividing a square 6 times by applying (a) the classical 2-point de Rham-Chaikin scheme, whic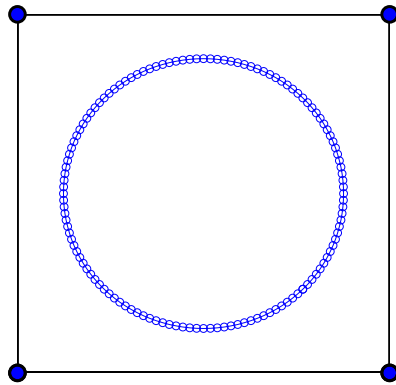h is linear, corner-cutting, and approximation; (b) the classical DLG 4-point interpolatory scheme; (c) the linear binary approximation scheme induced from the quintic cardinal B-spline N_6; and (d) the linear ternary approximation scheme induced from the quartic cardinal B-spline N_5.

(Chalmovianský and Jüttler [6]), *reproducing conics* (Beccari, et al. [2]), *circular precision* (Farin [14]), and *circle preserving* (Augsdörfer [1] and Romani [30]).

A brief review of typical linear and circular arc related schemes, together with 3-point circular-invariant schemes in (Lian, et al. [18]), is given in the following.

1.1   Classical Linear Subdivision Schemes

Most, if not all, classical linear subdivision schemes in the CAD/CAGD/CAM literature are not circular-invariant. Fig. 1 illustrates the results after subdividing a square 6 times by applying four typical linear subdivision schemes. It is categorized as *pseudo-circular* if it looks visually like a circle but in reality it is not. With the limiting curve being a piecewise quadratic polyno-

mial, Fig. 1(a) shows the pseudo-circular result from the classical 2-point corner-cutting linear *approximation* de Rham-Chaikin scheme (Chaikin [5]), i.e.,

$$\boldsymbol{\lambda}_{2k}^{(n+1)} = \frac{3}{4}\boldsymbol{\lambda}_{k-1}^{(n)} + \frac{1}{4}\boldsymbol{\lambda}_{k}^{(n)}, \tag{1}$$

$$\boldsymbol{\lambda}_{2k+1}^{(n+1)} = \frac{1}{4}\boldsymbol{\lambda}_{k-1}^{(n)} + \frac{3}{4}\boldsymbol{\lambda}_{k}^{(n)}, \quad k \in \mathbb{Z}; \quad n \in \mathbb{Z}_+, \tag{2}$$

where $\{\boldsymbol{\lambda}_{k}^{(n)} : k \in \mathbb{Z}\}$ and $\{\boldsymbol{\lambda}_{k}^{(n+1)} : k \in \mathbb{Z}\}$ are the vertices on the nth and $(n+1)^{\text{st}}$ level subdivisions. Fig. 1(b) demonstrates the results from the classical Dyn-Levin-Gregory (DLG) 4-point linear *interpolatory* subdivision scheme in (Dyn, et al. [9]), namely,

$$\boldsymbol{\lambda}_{2k}^{(n+1)} = \boldsymbol{\lambda}_{k}^{(n)}, \tag{3}$$

$$\boldsymbol{\lambda}_{2k+1}^{(n+1)} = -\frac{1}{16}\left(\boldsymbol{\lambda}_{k+2}^{(n)} + \boldsymbol{\lambda}_{k-1}^{(n)}\right) + \frac{9}{16}\left(\boldsymbol{\lambda}_{k+1}^{(n)} + \boldsymbol{\lambda}_{k}^{(n)}\right), \quad k \in \mathbb{Z}; \quad n \in \mathbb{Z}_+. \tag{4}$$

Fig. 1(c) corresponds to the 4-point binary linear approximation scheme induced from the quintic cardinal B-spline N_6 (Chui [7]), that is,

$$\boldsymbol{\lambda}_{2k}^{(n+1)} = \frac{1}{32}\left(\boldsymbol{\lambda}_{k+2}^{(n)} + \boldsymbol{\lambda}_{k-1}^{(n)}\right) + \frac{15}{32}\left(\boldsymbol{\lambda}_{k+1}^{(n)} + \boldsymbol{\lambda}_{k}^{(n)}\right), \tag{5}$$

$$\boldsymbol{\lambda}_{2k+1}^{(n+1)} = \frac{3}{16}\left(\boldsymbol{\lambda}_{k+2}^{(n)} + \boldsymbol{\lambda}_{k}^{(n)}\right) + \frac{5}{8}\boldsymbol{\lambda}_{k+1}^{(n)}, \quad k \in \mathbb{Z}; \quad n \in \mathbb{Z}_+. \tag{6}$$

Fig. 1(d) is from the 4-point ternary linear approximation scheme induced from the quartic cardinal B-spline N_5 (Chui [7]), or explicitly,

$$\boldsymbol{\lambda}_{3k}^{(n+1)} = \frac{5}{27}\left(\boldsymbol{\lambda}_{k+1}^{(n)} + \boldsymbol{\lambda}_{k-1}^{(n)}\right) + \frac{17}{27}\boldsymbol{\lambda}_{k}^{(n)}, \tag{7}$$

$$\boldsymbol{\lambda}_{3k+1}^{(n+1)} = \frac{1}{81}\boldsymbol{\lambda}_{k+2}^{(n)} + \frac{10}{27}\boldsymbol{\lambda}_{k+1}^{(n)} + \frac{5}{9}\boldsymbol{\lambda}_{k}^{(n)} + \frac{5}{81}\boldsymbol{\lambda}_{k-1}^{(n)}, \tag{8}$$

$$\boldsymbol{\lambda}_{3k+2}^{(n+1)} = \frac{5}{81}\boldsymbol{\lambda}_{k+2}^{(n)} + \frac{5}{9}\boldsymbol{\lambda}_{k+1}^{(n)} + \frac{10}{27}\boldsymbol{\lambda}_{k}^{(n)} + \frac{1}{81}\boldsymbol{\lambda}_{k-1}^{(n)}, \quad k \in \mathbb{Z}; \quad n \in \mathbb{Z}_+. \tag{9}$$

With the initial polygon as a square, for instance, the limiting curves of all four of these linear schemes in (1)–(2), (3)–(4), (5)–(6), and (7)–(9), are not circles. A simple proof is given in Appendix A.

1.2   Rational Bézier Curve

It is also known that there is a unique rational Bézier curve, depicted as an arc of a circle that is tangent to an isosceles triangle (Piegl [27], Piegl & Tiller [28], Farin [11], Farin [12], Farin [14]) which can be written as

$$\boldsymbol{p}(t) = \frac{\boldsymbol{\lambda}_0 B_{0,2}(t) + w_1\boldsymbol{\lambda}_1 B_{1,2}(t) + \boldsymbol{\lambda}_2 B_{2,2}(t)}{B_{0,2}(t) + w_1 B_{1,2}(t) + B_{2,2}(t)} = \frac{\boldsymbol{\lambda}_0(1-t)^2 + 2w_1\boldsymbol{\lambda}_1 t(1-t) + \boldsymbol{\lambda}_2 t^2}{(1-t)^2 + 2w_1 t(1-t) + t^2}, \; t \in [0,1], \tag{10}$$

where, as shown in Fig. 2, $\boldsymbol{\lambda}_0$, $\boldsymbol{\lambda}_1$, and $\boldsymbol{\lambda}_2$ are the three vertices of an isosceles triangle with two equal angles at vertices $\boldsymbol{\lambda}_0$ and $\boldsymbol{\lambda}_2$; $B_{i,n}$ is the ith Bernstein polynomial of degree n, namely,

$$B_{i,n}(t) = \binom{n}{i}t^i(1-t)^{n-i}, \quad i = 0, \ldots, n; \quad n \in \mathbb{Z}_+; \tag{11}$$

Applications and Applied Mathematics: An International Journal (AAM), Vol. 7 [2012], Iss. 1, Art. 30

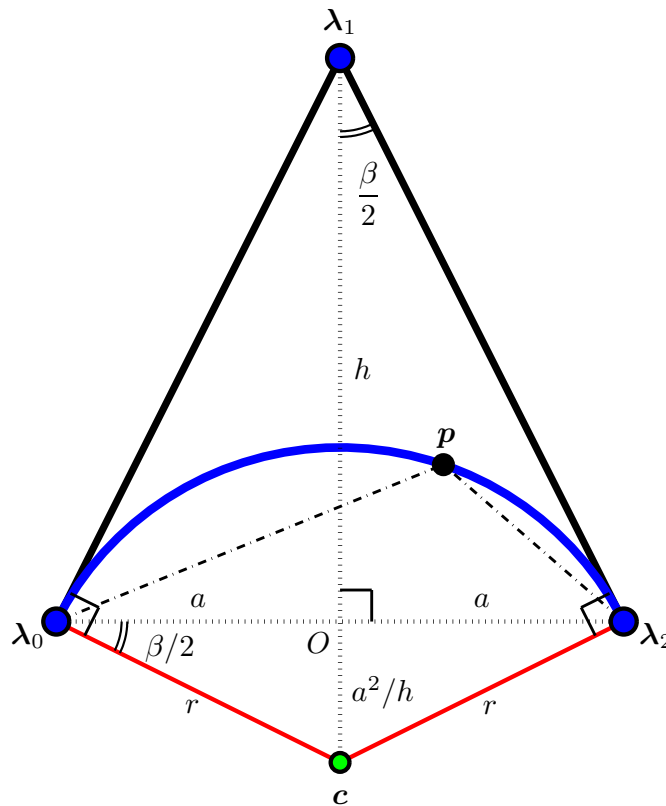AAM: Intern. J., Vol. 7, Issue 1 (June 2012)   467

Fig. 2.   An illustration for an arc of a circle as a rational quadratic Bézier curve.

w_1 is the *weight* at the vertex $\boldsymbol{\lambda}_1$:

$$w_1 = \sin\frac{\beta}{2} = \frac{a}{\sqrt{a^2 + h^2}}, \tag{12}$$

with h the height on the base of the isosceles triangle and β the angle at $\boldsymbol{\lambda}_1$; the distance from O to the center $\boldsymbol{c}$ of the circle is a^2/h; and the radius r of the circle is

$$r = a\sec\frac{\beta}{2} = \frac{a\sqrt{a^2 + h^2}}{h}. \tag{13}$$

By defining

$$\text{chord}(t) = \frac{\|\boldsymbol{p}(t) - \boldsymbol{\lambda}_0\|}{\|\boldsymbol{p}(t) - \boldsymbol{\lambda}_0\| + \|\boldsymbol{p}(t) - \boldsymbol{\lambda}_2\|}, \tag{14}$$

an interesting proof was given in (Farin[13]) by using *Mathematica* that

$$\text{chord}(t) = t, \quad t \in [0, 1]. \tag{15}$$

A direct proof of (15) is given in Appendix B.

With $\widetilde{\boldsymbol{\lambda}}_0 = (\boldsymbol{\lambda}_0 + \boldsymbol{\lambda}_1)/2$ and $\widetilde{\boldsymbol{\lambda}}_2 = (\boldsymbol{\lambda}_1 + \boldsymbol{\lambda}_2)/2$ in Fig. 4, the subdivision scheme induced from the rational Bézier quadratics is

$$\boldsymbol{\lambda}_{2k-1}^{(n+1)} = \frac{1-s_k}{2}\boldsymbol{\lambda}_{k-1}^{(n)} + \frac{1+s_k}{2}\boldsymbol{\lambda}_k^{(n)}, \tag{16}$$

$$\boldsymbol{\lambda}_{2k}^{(n+1)} = \frac{1+s_k}{2}\boldsymbol{\lambda}_k^{(n)} + \frac{1-s_k}{2}\boldsymbol{\lambda}_{k+1}^{(n)}, \quad k \in \mathbb{Z}; \quad n \in \mathbb{Z}_+, \tag{17}$$

where

$$s_k = \frac{\sin\frac{\beta_k}{2}}{1+\sin\frac{\beta_k}{2}}, \tag{18}$$

with $\beta_k = \angle\boldsymbol{\lambda}_{k-1}^{(n)}\boldsymbol{\lambda}_k^{(n)}\boldsymbol{\lambda}_{k+1}^{(n)}$. Observe that this nonlinear subdivision scheme is not circular-invariant for both isosceles and scalene triangles, as shown in Fig. 5(a)–5(b).

1.3   Biarc Curves and Biarc Circular Splines

To generalize the circular arc from equal-length legs to nonequal-length legs, *biarc* and *circular splines* were introduced in (Bolton [3], Moreton & Parkinson [23], Meek & Walton [20], Hoschek [17], Schönherr [31], Ong, et al. [26], Wong, et al. [32], Nasri, et al. [25], Piegl & Tiller [29], Yang & Chen [33], Nasri & Farin [24]).

There are C- and S-shaped biarcs. Fig. 3 displays a variety of C- and S-shaped biarcs. Take Fig. 3(a) as an example. With the parameter α_1 defined by

$$\alpha_1 = \frac{\|\boldsymbol{\mu}_0 - \boldsymbol{\lambda}_2\|}{\|\boldsymbol{\lambda}_1 - \boldsymbol{\lambda}_2\|},$$

it is easy to see that

$$\alpha_2 = \frac{\|\boldsymbol{\lambda}_2 - \boldsymbol{\mu}_1\|}{\|\boldsymbol{\lambda}_2 - \boldsymbol{\lambda}_3\|} = \frac{\|\boldsymbol{\lambda}_1 - \boldsymbol{\lambda}_2\|}{\|\boldsymbol{\lambda}_2 - \boldsymbol{\lambda}_3\|}\alpha_1,$$

$$\alpha_3 = \frac{\|\boldsymbol{\lambda}_3 - \boldsymbol{\mu}_2\|}{\|\boldsymbol{\lambda}_3 - \boldsymbol{\lambda}_4\|} = \frac{\|\boldsymbol{\lambda}_2 - \boldsymbol{\lambda}_3\| - \|\boldsymbol{\lambda}_1 - \boldsymbol{\lambda}_2\|\alpha_1}{\|\boldsymbol{\lambda}_3 - \boldsymbol{\lambda}_4\|}.$$

So a reasonable choice for $\alpha_1 \in (0,1)$ gives either a C-shaped or S-shaped biarc. Fig. 3(a) is with $\alpha_1 = .5$ while Fig. 3(b) is with $\alpha_1 = .25$. Fig. 3(c) is when the two centers of the circular arcs coincide, to be named *uni-arc*. This requirement determines the unique value of α_1. Fig. 3(f) demonstrate a uni-arc for an L-shaped initial 4-point data set.
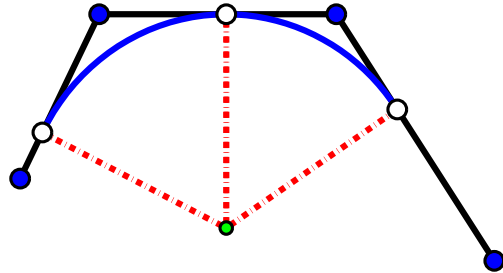
Fig. 4, on the other hand, shows a C-shaped biarc structure from 3 vertices, where $\|\widetilde{\boldsymbol{\lambda}}_0 - \boldsymbol{\lambda}_1\| \neq \|\widetilde{\boldsymbol{\lambda}}_2 - \boldsymbol{\lambda}_1\|$, $\boldsymbol{\mu}_0 = \widetilde{\boldsymbol{\lambda}}_0 + \alpha(\boldsymbol{\lambda}_1 - \widetilde{\boldsymbol{\lambda}}_0)$ for some $0 < \alpha < 1$, $\boldsymbol{\mu}_2 = \boldsymbol{\lambda}_1 + \beta(\widetilde{\boldsymbol{\lambda}}_2 - \boldsymbol{\lambda}_1)$ for some $0 < \beta < 1$. The three collinear points $\boldsymbol{\mu}_0$, $\boldsymbol{\mu}_1$, and $\boldsymbol{\mu}_2$ are determined by $\|\widetilde{\boldsymbol{\lambda}}_0 - \boldsymbol{\mu}_0\| = \|\boldsymbol{\mu}_0 - \boldsymbol{\mu}_1\|$; $\|\widetilde{\boldsymbol{\lambda}}_2 - \boldsymbol{\mu}_2\| = \|\boldsymbol{\mu}_1 - \boldsymbol{\mu}_2\|$; and $\alpha + \beta = 1$, so that $\widetilde{\boldsymbol{\lambda}}_0 p_1 \boldsymbol{\mu}_1$ is a circular arc with radius r_1 and center at $\boldsymbol{c}_1$, and $\boldsymbol{\mu}_1 p_2 \widetilde{\boldsymbol{\lambda}}_2$ is a circular arc with radius r_2 and center at $\boldsymbol{c}_2$. The line $\overline{\widetilde{\boldsymbol{\lambda}}_0 \boldsymbol{\lambda}_1}$ is tangent to the arc $\widetilde{\boldsymbol{\lambda}}_0 p_1 \boldsymbol{\mu}_1$ at $\widetilde{\boldsymbol{\lambda}}_0$, the line $\overline{\widetilde{\boldsymbol{\lambda}}_2 \boldsymbol{\lambda}_1}$ is tangent to the arc $\boldsymbol{\mu}_1 p_2 \widetilde{\boldsymbol{\lambda}}_2$ at $\widetilde{\boldsymbol{\lambda}}_2$, while $\overline{\boldsymbol{\mu}_0 \boldsymbol{\mu}_2}$ is tangent to both arcs at $\boldsymbol{\mu}_1$. It is clear that the two circular arcs coincide if and only if $\|\widetilde{\boldsymbol{\lambda}}_0 - \boldsymbol{\lambda}_1\| = \|\widetilde{\boldsymbol{\lambda}}_2 - \boldsymbol{\lambda}_1\|$.

Applications and Applied Mathematics: An International Journal (AAM), Vol. 7 [2012], Iss. 1, Art. 30

AAM: Intern. J., Vol. 7, Issue 1 (June 2012)   469
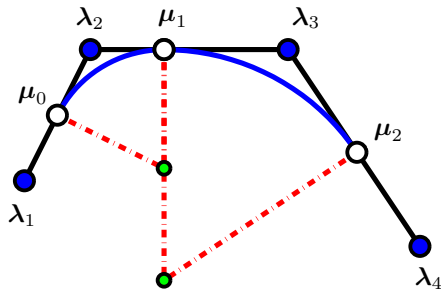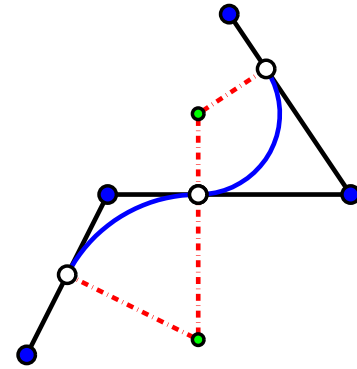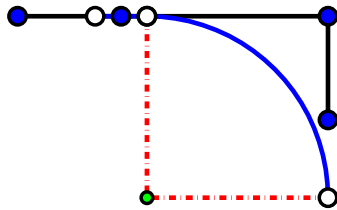
(a) A C-shaped biarc with $\alpha_1 = .5$
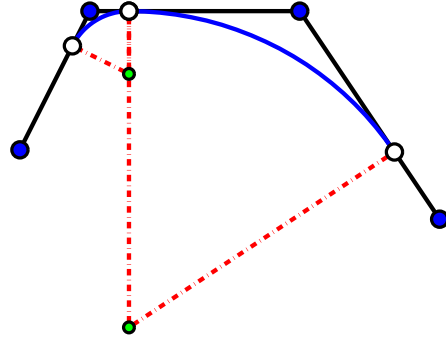
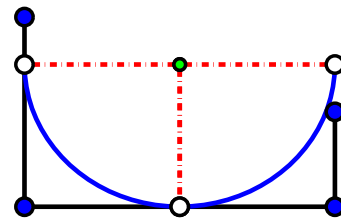(b) A C-shaped biarc with $\alpha_1 = .25$

(c) A C-shaped biarc becomes a uni-arc (this paper)

(d) An S-shaped biarc with $\alpha_1 = .5$

(e) A special C-shaped biarc with $\alpha_1 = .5$

(f) A biarc turns to uni-arc too

Fig. 3.   Illustrations of C- and S-shaped biarcs. In particular, (c) shows a C-shaped biarc that becomes a uni-arc (this paper); (e) indicates a special C-shaped biarcs with $\alpha_1 = .25$, where the first set of 3 vertices are collinear; and (f) displays a half-circle induced from an L-shaped initial data set.
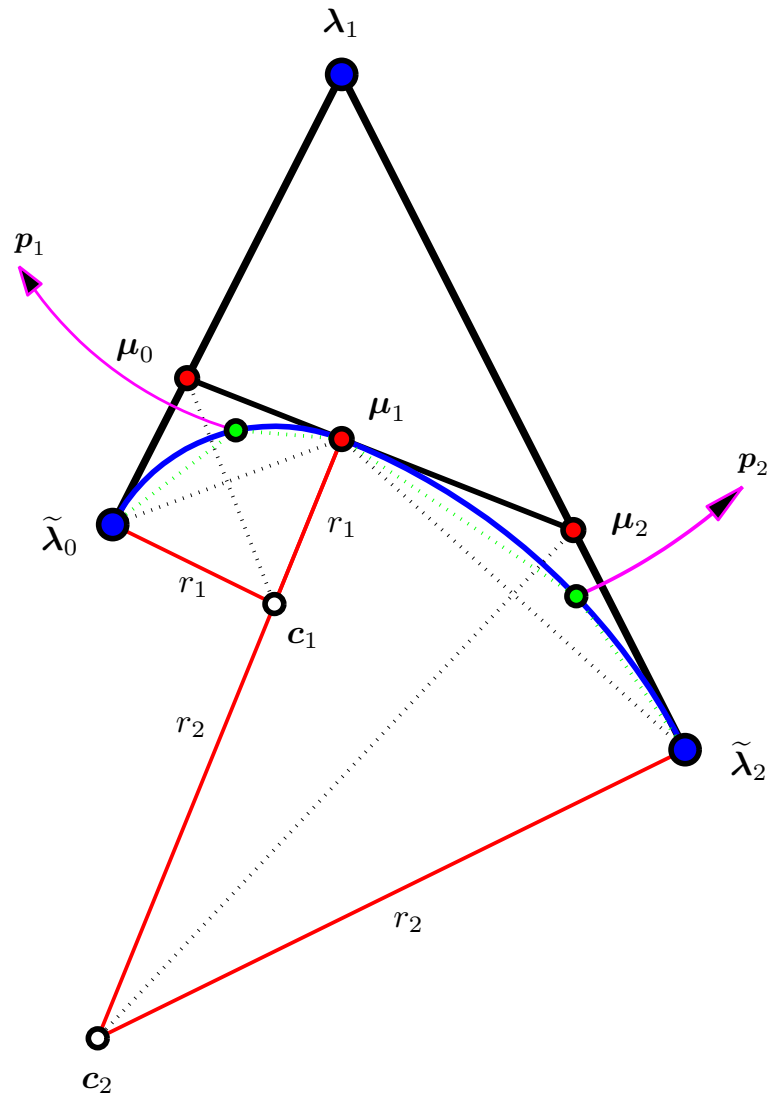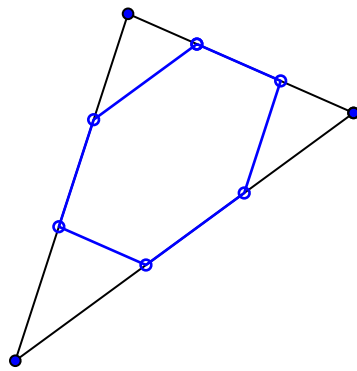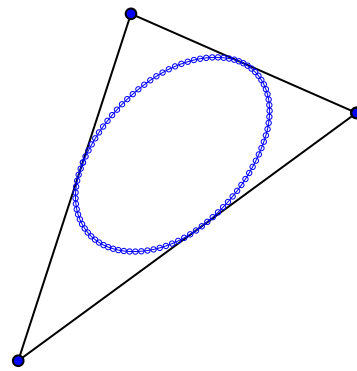
Fig. 4.   An illustration of a biarc from 3 vertices.

Applications and Applied Mathematics: An International Journal (AAM), Vol. 7 [2012], Iss. 1, Art. 30

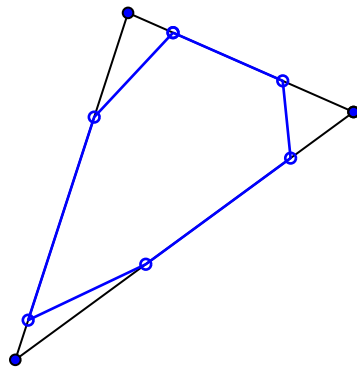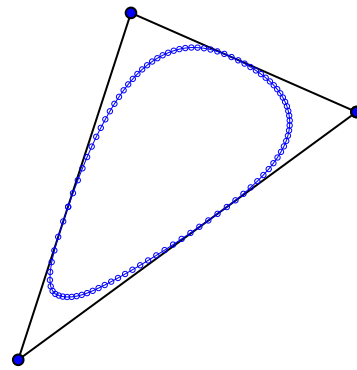AAM: Intern. J., Vol. 7, Issue 1 (June 2012) 471

(a) After 1 subdivision

(b) After 5 subdivisions

(c) After 1 subdivision

(d) After 5 subdivisions

Fig. 5. Illustrations for subdividing a scalene triangle. (a) The initial scalene triangle & after 1 subdivision by applying (16)–(18). (b) The scalene triangle & after 5 subdivisions by applying (16)–(18). (c) The initial scalene triangle & after 1 subdivision by applying (19)–(21). (d) The scalene triangle & after 5 subdivisions by applying (19)–(21).

With all the same conditions except $\alpha = \beta$, Nasri, et al. introduced a biarc construction in [25]. More precisely, with $\widetilde{\boldsymbol{\lambda}}_0 = (\boldsymbol{\lambda}_0 + \boldsymbol{\lambda}_1)/2$ and $\widetilde{\boldsymbol{\lambda}}_2 = (\boldsymbol{\lambda}_1 + \boldsymbol{\lambda}_2)/2$ in Fig. 4, the subdivision scheme is explicitly given by

$$\boldsymbol{\lambda}_{2k-1}^{(n+1)} = \frac{1 - \tau_k}{2} \boldsymbol{\lambda}_{k-1}^{(n)} + \frac{1 + \tau_k}{2} \boldsymbol{\lambda}_k^{(n)}, \tag{19}$$

$$\boldsymbol{\lambda}_{2k}^{(n+1)} = \left(1 - \frac{\tau_k}{2}\right) \boldsymbol{\lambda}_k^{(n)} + \frac{\tau_k}{2} \boldsymbol{\lambda}_{k+1}^{(n)}, \quad k \in \mathbb{Z}; \quad n \in \mathbb{Z}_+, \tag{20}$$

where

$$\tau_k = \frac{\|\boldsymbol{\lambda}_{k-1}^{(n)} - \boldsymbol{\lambda}_k^{(n)}\| + \|\boldsymbol{\lambda}_k^{(n)} - \boldsymbol{\lambda}_{k+1}^{(n)}\|}{\|\boldsymbol{\lambda}_{k-1}^{(n)} - \boldsymbol{\lambda}_k^{(n)}\| + \|\boldsymbol{\lambda}_k^{(n)} - \boldsymbol{\lambda}_{k+1}^{(n)}\| + \|\boldsymbol{\lambda}_{k+1}^{(n)} - \boldsymbol{\lambda}_{k-1}^{(n)}\|}. \tag{21}$$

However, it is also clear that both schemes in (16)–(17) and (19)–(20) are not circular-invariant for both isosceles and scalene triangles, as demonstrated in Fig. 5(b) and Fig. 5(d) for a scalene triangle.

(a) Ternary interpolatory   (b) Binary approximation
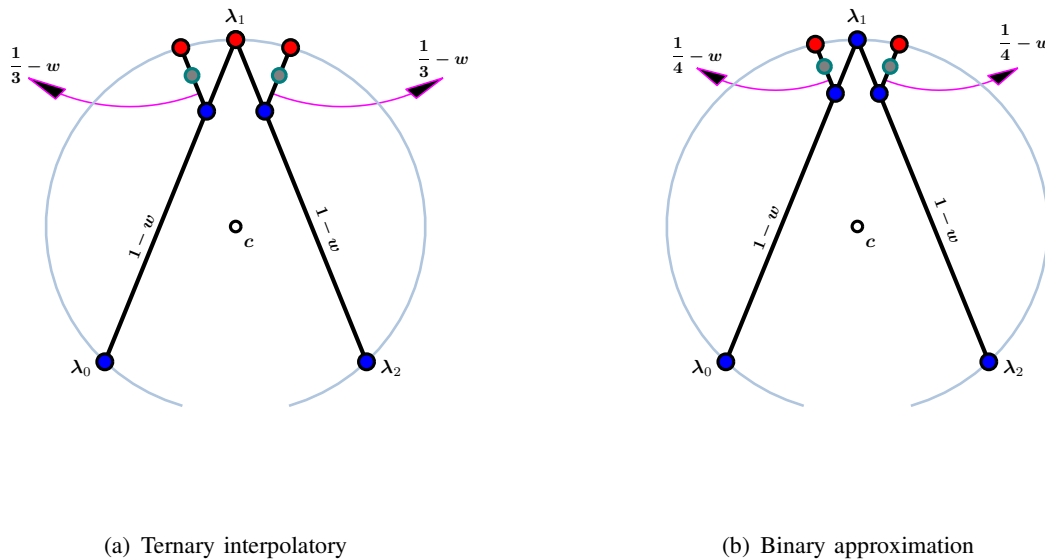
Fig. 6.   Two families of nonlinear 3-point circular-invariant subdivision schemes in (Lian, et al. [18]), given here by (22) and (23). The two segments are partitioned based upon the ratio of $w : (1 - w)$. A new line is drawn from each partitioned point in such a way that the line is parallel to the other line segment. The intersections of the two new lines with the circle (formed by the three old vertices) are the new vertices for the next level (marked solid and red). Here the intersections on the circle are chosen to be above the lines formed by $\overline{\lambda_0 \lambda_1}$ and $\overline{\lambda_2 \lambda_1}$, respectively. (a) The ternary interpolatory scheme, where the two gray dots are the new vertices generated from the linear ternary interpolatory subdivision scheme when $\xi_k^{(n)} = \eta_k^{(n)} = 1/3 - w$. They are plotted for reference only. (b) The binary approximation scheme, where the two gray dots are the new vertices generated from the linear binary approximation subdivision scheme when $\xi_k^{(n)} = \eta_k^{(n)} = 1/4 - w$. They are plotted for reference as well.
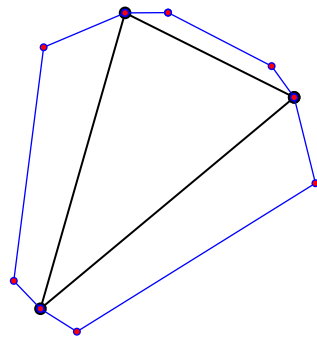
1.4   3-Point Nonlinear Circular-Invariant Schemes

Two families of 3-point nonlinear circular-invariant schemes were established in (Lian, et al. [18]), where the first family was ternary interpolatory and the second was binary approximation. In details, the ternary schemes were given by
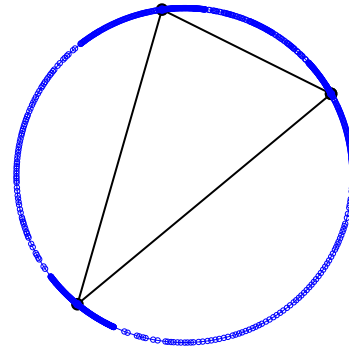
$$\boldsymbol{\lambda}_{3k-1}^{(n+1)} = w\boldsymbol{\lambda}_{k-1}^{(n)} + (1-w)\boldsymbol{\lambda}_k^{(n)} + \xi_k^{(n)}(\boldsymbol{\lambda}_k^{(n)} - \boldsymbol{\lambda}_{k+1}^{(n)}),$$
$$\boldsymbol{\lambda}_{3k}^{(n+1)} = \boldsymbol{\lambda}_k^{(n)},$$
$$\boldsymbol{\lambda}_{3k+1}^{(n+1)} = (1-w)\boldsymbol{\lambda}_k^{(n)} + w\boldsymbol{\lambda}_{k+1}^{(n)} + \eta_k^{(n)}(\boldsymbol{\lambda}_k^{(n)} - \boldsymbol{\lambda}_{k-1}^{(n)}), \qquad k \in \mathbb{Z}; \quad n \in \mathbb{Z}_+, \qquad (22)$$

where both $\xi_k^{(n)}$ and $\eta_k^{(n)}$ are so chosen that both $\boldsymbol{\lambda}_{3k-1}^{(n+1)}$ and $\boldsymbol{\lambda}_{3k+1}^{(n+1)}$ in (22) are two intersections of the circle formed by $\boldsymbol{\lambda}_{k-1}^{(n)}$, $\boldsymbol{\lambda}_k^{(n)}$, and $\boldsymbol{\lambda}_{k+1}^{(n)}$; and w is a tension parameter on $(0, 1)$. See Fig.6 for a geometric illustration. The binary schemes were given by

$$\boldsymbol{\lambda}_{2k-1}^{(n+1)} = w\boldsymbol{\lambda}_{k-1}^{(n)} + (1-w)\boldsymbol{\lambda}_k^{(n)} + \xi_k^{(n)}(\boldsymbol{\lambda}_k^{(n)} - \boldsymbol{\lambda}_{k+1}^{(n)}),$$
$$\boldsymbol{\lambda}_{2k}^{(n+1)} = (1-w)\boldsymbol{\lambda}_k^{(n)} + w\boldsymbol{\lambda}_{k+1}^{(n)} + \eta_k^{(n)}(\boldsymbol{\lambda}_k^{(n)} - \boldsymbol{\lambda}_{k-1}^{(n)}), \qquad k \in \mathbb{Z}; \quad n \in \mathbb{Z}_+, \qquad (23)$$

Applications and Applied Mathematics: An International Journal (AAM), Vol. 7 [2012], Iss. 1, Art. 30

AAM: Intern. J., Vol. 7, Issue 1 (June 2012)   473

(a) Ternary Interpolatory

(b) After 5 ternary subdivisions
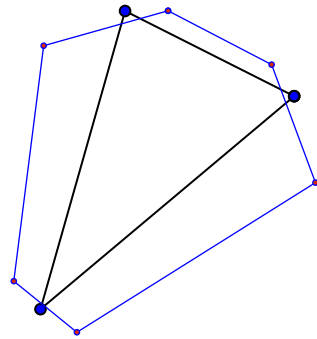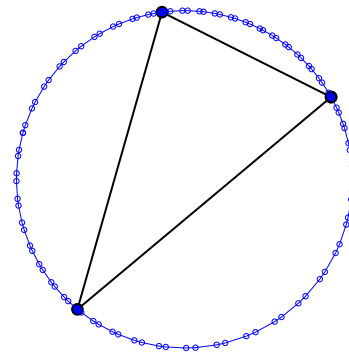
(c) Binary Approximation (or corner-cutting)

(d) After 5 binary subdivisions

Fig. 7. Nonlinear 3-point circular-invariant ternary interpolatory scheme in (22) and binary approximation scheme in (23) are applied to an initial polygon as a scalene triangle. (a) initial scalene triangle and polygon after 1 subdivision of scheme in(22); (b) initial scalene triangle and polygon after 5 subdivisions of scheme in(22); (c) initial scalene triangle and polygon after 1 subdivision of scheme in(23); and (d) initial scalene triangle and polygon after 5 subdivisions of scheme in(23).

with both $\xi_k^{(n)}$ and $\eta_k^{(n)}$ being chosen in the same manner as in ternary interpolatory schemes in (22), and w is also a tension parameter on $(0, 1)$. The illustration in Fig.6 is still valid for the binary schemes except for the three old vertices are not interpolatory (or kept for new broken lines).

An example of these two schemes applied to a scalene triangle is given by Fig.7.

Here is the outline of this paper. Our new 4-point nonlinear circular-invariant subdivision scheme will be established and illustrated in detail in Section 2. The convergence of our new nonlinear subdivision scheme for curve design will be proved in Section 3. Some examples will be explicitly demonstrated in Section 4, while the conclusion constitutes Section 5. The Appendix entails two
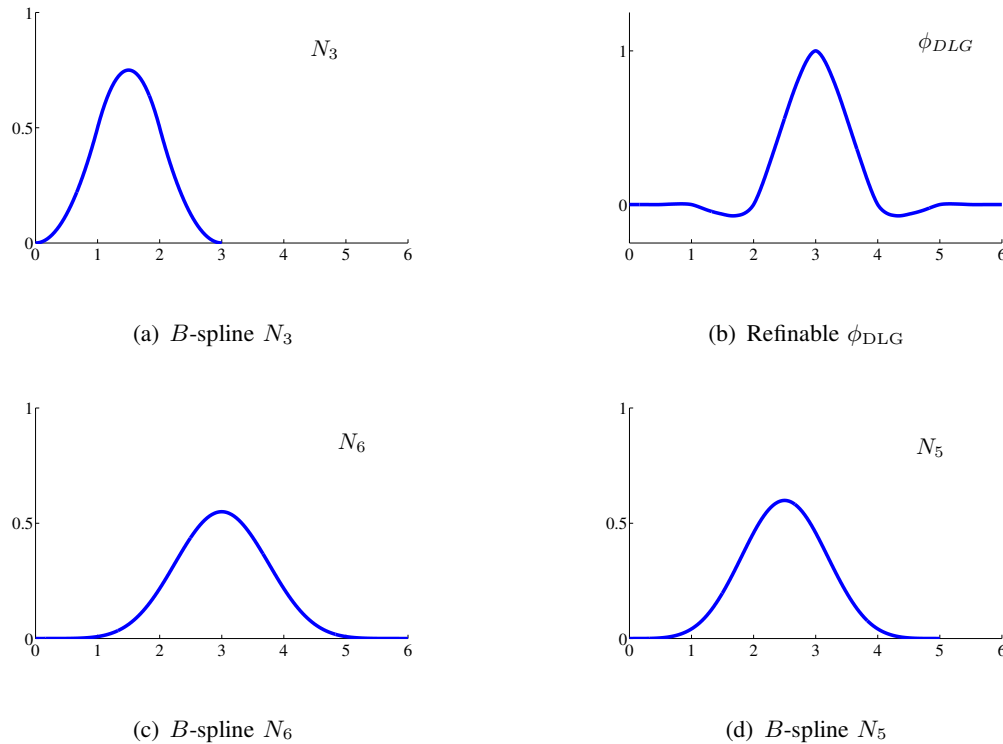
(a) B-spline N_3

(b) Refinable ϕ_{DLG}

(c) B-spline N_6

(d) B-spline N_5

Fig. 8.   Basis functions in (36)–(39) (a) the 3rd-order cardinal B-spline N_3; (b) the DLG refinable function ϕ_{DLG}; (c) the 6th-order cardinal B-spline N_6; and (d) the quartic cardinal B-spline N_5.

simple proofs.

2.   A New Nonlinear Circular-Invariant Subdivision Scheme

As we have verified for the four linear schemes in Section 1.1, with its simple proof given in Appendix A, the non-existence of a linear scheme that is circular-invariant in the generic setting can be proved analogously. Hence-forward, a circular-invariant scheme must be nonlinear.

To facilitate the illustration of our new nonlinear circular-invariant scheme, we introduce some notations first. See Fig. 9 for geometric details, which is indeed a special C-shaped biarc when the two centers of the circles coincide. See Fig. 3(c) too.

Let $\boldsymbol{\lambda}_{k-1}^{(n)}$, $\boldsymbol{\lambda}_{k}^{(n)}$, $\boldsymbol{\lambda}_{k+1}^{(n)}$, and $\boldsymbol{\lambda}_{k+2}^{(n)}$ be 4 consecutive vertices on the nth-level subdivision. Let $\boldsymbol{\lambda}_{2k}^{(n+1)}$ and $\boldsymbol{\lambda}_{2k+1}^{(n+1)}$ be the two new vertices on the $(n+1)^{\mathrm{st}}$-level subdivision, which are to be nonlinearly determined by the 4 n^{th}-level vertices $\boldsymbol{\lambda}_{k-1}^{(n)}$, $\boldsymbol{\lambda}_{k}^{(n)}$, $\boldsymbol{\lambda}_{k+1}^{(n)}$, and $\boldsymbol{\lambda}_{k+2}^{(n)}$. See Fig. 9 for geometric details.

Here is a detailed step-by-step description of our algorithm.

(1) Bisect the angle $\alpha_{k}^{(n)}$ formed by the three vertices $\boldsymbol{\lambda}_{k-1}^{(n)}$, $\boldsymbol{\lambda}_{k}^{(n)}$, and $\boldsymbol{\lambda}_{k+1}^{(n)}$, and bisect the angle $\alpha_{k+1}^{(n)}$ formed by the three vertices $\boldsymbol{\lambda}_{k}^{(n)}$, $\boldsymbol{\lambda}_{k+1}^{(n)}$, and $\boldsymbol{\lambda}_{k+2}^{(n)}$.

(2) Denote by $\mathbf{c}_{k}^{(n)}$ the intersection of the two bisection lines in (1). Then the distance from

Applications and Applied Mathematics: An International Journal (AAM), Vol. 7 [2012], Iss. 1, Art. 30

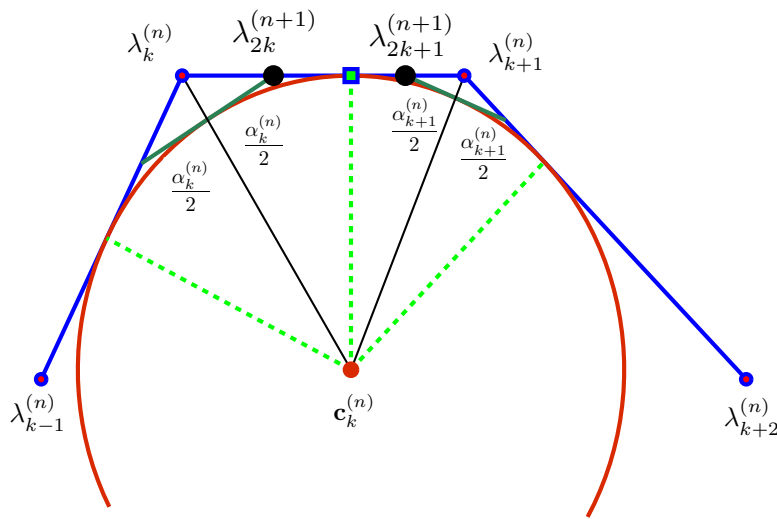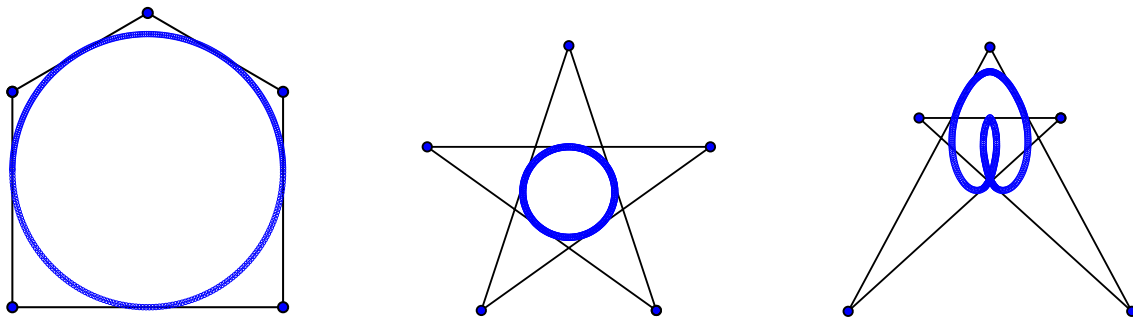AAM: Intern. J., Vol. 7, Issue 1 (June 2012) 475

Fig. 9. An illustration of our new nonlinear circular-invariant subdivision scheme. Four n^{th}-level vertices are $\boldsymbol{\lambda}_{k-1}^{(n)}$, $\boldsymbol{\lambda}_{k}^{(n)}$, $\boldsymbol{\lambda}_{k+1}^{(n)}$, and $\boldsymbol{\lambda}_{k+2}^{(n)}$; two new or $(n+1)^{\text{st}}$-level vertices are $\boldsymbol{\lambda}_{2k}^{(n+1)}$ and $\boldsymbol{\lambda}_{2k+1}^{(n+1)}$.

(a) A particular irregular polygon   (b) A regular star polygon   (c) An irregular star polygon

Fig. 10. (a) Our scheme is applied to an irregular pentagon that has an incirle that touches all sides. The limiting curve is circular-invariant. (b) Our scheme is applied to a regular star polygon and yields an incirle. (c) Our scheme is applied to an irregular star polygon and yields a self-intersecting double loop.

$\mathbf{c}_k^{(n)}$ to the three straight lines, formed by the three segments

$$\overline{\boldsymbol{\lambda}_{k-1}^{(n)}\,\boldsymbol{\lambda}_{k}^{(n)}}, \quad \overline{\boldsymbol{\lambda}_{k}^{(n)}\,\boldsymbol{\lambda}_{k+1}^{(n)}}, \quad \overline{\boldsymbol{\lambda}_{k+1}^{(n)}\,\boldsymbol{\lambda}_{k+2}^{(n)}}, \tag{24}$$

will be the same. In other words, there is a unique circle inscribed with the three straight lines in (24).

(3) Draw the tangent line to the circle that is perpendicular to the line formed by $\mathbf{c}_k^{(n)}$ and $\boldsymbol{\lambda}_k^{(n)}$. The intersection of this tangent line with the line segment $\overline{\boldsymbol{\lambda}_k^{(n)}\,\boldsymbol{\lambda}_{k+1}^{(n)}}$ will be a new vertex, to be named as $\boldsymbol{\lambda}_{2k}^{(n+1)}$. Similarly, draw the tangent line to the circle that is perpendicular to the line formed by $\mathbf{c}_k^{(n)}$ and $\boldsymbol{\lambda}_{k+1}^{(n)}$. The intersection of this tangent line with the line
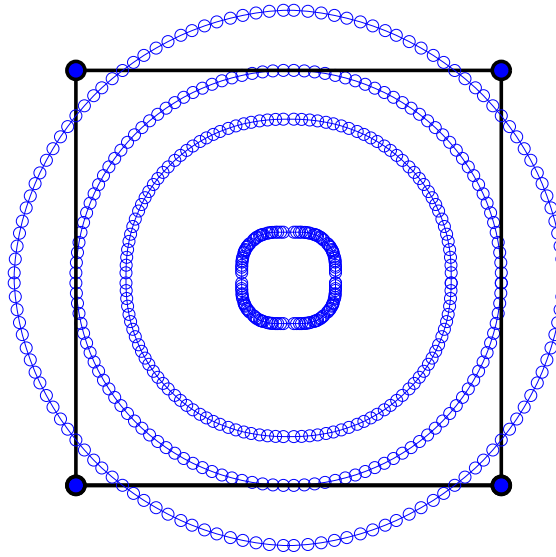
Fig. 11.   Illustration of our scheme with adjustable radii: applied to a square after 5 subdivisions and with uniform parameter κ_k in (28) being, from inside out, .5, .9, 1, and 1.1, respectively.

segment $\overline{\boldsymbol{\lambda}_k^{(n)} \boldsymbol{\lambda}_{k+1}^{(n)}}$ will be another new vertex, to be named as $\boldsymbol{\lambda}_{2k+1}^{(n+1)}$.

(4) Repeat the procedure for all sets of 4 consecutive vertices on the nth-level, all vertices for the $(n+1)^{\text{st}}$-level can be formed.

Observe that, first, each pair of new vertices $\boldsymbol{\lambda}_{2k}^{(n+1)}$ and $\boldsymbol{\lambda}_{2k+1}^{(n+1)}$ generated in 3) are determined by two old vertices $\boldsymbol{\lambda}_k^{(n)}$ and $\boldsymbol{\lambda}_{k+1}^{(n)}$, together with two angles $\alpha_k^{(n)}$ and $\alpha_{k+1}^{(n)}$, which are the directions of the line formed by $\boldsymbol{\lambda}_{k-1}^{(n)}$ and $\boldsymbol{\lambda}_k^{(n)}$, and the line formed by $\boldsymbol{\lambda}_{k+1}^{(n)}$ and $\boldsymbol{\lambda}_{k+2}^{(n)}$. In other words, the two new vertices are independent of the lengths $\overline{\boldsymbol{\lambda}_{k-1}^{(n)} \boldsymbol{\lambda}_k^{(n)}}$ and $\overline{\boldsymbol{\lambda}_{k+1}^{(n)} \boldsymbol{\lambda}_{k+2}^{(n)}}$. Second, it is straightforward from the construction that our new nonlinear scheme is indeed circular-invariant for any regular polygon. It is also circular-invariant for a scalene triangle. It is also true whenever there exists an incircle that touches all edges of the initial polygon, as illustrated by Fig. 10. Our new scheme can also be applied to star polygons, as illustrated in Fig. 10(b) and Fig. 10(c). Third, our scheme can be written as

$$\boldsymbol{\lambda}_{2k}^{(n+1)} = \left(1 - \omega_{k,1}^{(n)}\right) \boldsymbol{\lambda}_k^{(n)} + \omega_{k,1}^{(n)} \boldsymbol{\lambda}_{k+1}^{(n)}, \tag{25}$$

$$\boldsymbol{\lambda}_{2k+1}^{(n+1)} = \omega_{k,2}^{(n)} \boldsymbol{\lambda}_k^{(n)} + \left(1 - \omega_{k,2}^{(n)}\right) \boldsymbol{\lambda}_{k+1}^{(n)}, \quad k \in \mathbb{Z}; \quad n \in \mathbb{Z}_+, \tag{26}$$

where $\omega_{k,1}^{(n)}$ and $\omega_{k,2}^{(n)}$ are *nonlinear* functions of *four* vertices $\boldsymbol{\lambda}_{k-1}^{(n)}, \boldsymbol{\lambda}_k^{(n)}, \boldsymbol{\lambda}_{k+1}^{(n)}$, and $\boldsymbol{\lambda}_{k+2}^{(n)}$, satisfying $0 < \omega_{k,1}^{(n)}, \omega_{k,2}^{(n)} < 1$. Finally, to evaluate $\boldsymbol{\lambda}_{2k}^{(n+1)}$ and $\boldsymbol{\lambda}_{2k+1}^{(n+1)}$ in (25)–(26), let c, a, and b be the lengths of the three segments in (24), i.e.,

$$c = \overline{\boldsymbol{\lambda}_{k-1}^{(n)} \boldsymbol{\lambda}_k^{(n)}}, \quad a = \overline{\boldsymbol{\lambda}_k^{(n)} \boldsymbol{\lambda}_{k+1}^{(n)}}, \quad b = \overline{\boldsymbol{\lambda}_{k+1}^{(n)} \boldsymbol{\lambda}_{k+2}^{(n)}};$$

Applications and Applied Mathematics: An International Journal (AAM), Vol. 7 [2012], Iss. 1, Art. 30

AAM: Intern. J., Vol. 7, Issue 1 (June 2012)   477

let d_{13} and d_{24} be the lengths of the line segments from $\boldsymbol{\lambda}_{k-1}^{(n)}$ to $\boldsymbol{\lambda}_{k+1}^{(n)}$ and from $\boldsymbol{\lambda}_k^{(n)}$ to $\boldsymbol{\lambda}_{k+2}^{(n)}$, that is,

$$d_{13} = \overline{\boldsymbol{\lambda}_{k-1}^{(n)}\,\boldsymbol{\lambda}_{k+1}^{(n)}}, \quad d_{14} = \overline{\boldsymbol{\lambda}_k^{(n)}\,\boldsymbol{\lambda}_{k+2}^{(n)}};$$

let (u, v) be the intersection of the perpendicular line from $\mathbf{c}_k^{(n)}$ to the segment $\overline{\boldsymbol{\lambda}_k^{(n)}\,\boldsymbol{\lambda}_{k+1}^{(n)}}$. Then, in terms of $\alpha_k^{(n)}$ and $\alpha_{k+1}^{(n)}$,

$$\boldsymbol{\lambda}_{2k}^{(n+1)} = \frac{1}{1 + \sin\left(\alpha_k^{(n)}/2\right)} \begin{bmatrix} u \\ v \end{bmatrix} + \frac{\sin\left(\alpha_k^{(n)}/2\right)}{1 + \sin\left(\alpha_k^{(n)}/2\right)} \boldsymbol{\lambda}_k^{(n)},$$

$$\boldsymbol{\lambda}_{2k+1}^{(n+1)} = \frac{1}{1 + \sin\left(\alpha_{k+1}^{(n)}/2\right)} \begin{bmatrix} u \\ v \end{bmatrix} + \frac{\sin\left(\alpha_{k+1}^{(n)}/2\right)}{1 + \sin\left(\alpha_{k+1}^{(n)}/2\right)} \boldsymbol{\lambda}_{k+1}^{(n)},$$

with $\sin\left(\alpha_k^{(n)}/2\right)$ and $\sin\left(\alpha_{k+1}^{(n)}/2\right)$ formulated by

$$\sin\frac{\alpha_k^{(n)}}{2} = \sqrt{\frac{d_{13}^2 - (a-c)^2}{4ac}}, \quad \sin\frac{\alpha_{k+1}^{(n)}}{2} = \sqrt{\frac{d_{24}^2 - (a-b)^2}{4ab}}.$$

The algorithm performs perfectly well if each set of 4 consecutive vertices $\boldsymbol{\lambda}_{k-1}^{(n)}$, $\boldsymbol{\lambda}_k^{(n)}$, $\boldsymbol{\lambda}_{k+1}^{(n)}$, and $\boldsymbol{\lambda}_{k+2}^{(n)}$, is *locally convex*, meaning both vertices $\boldsymbol{\lambda}_{k-1}^{(n)}$ and $\boldsymbol{\lambda}_{k+2}^{(n)}$ are on the same side of the line formed by $\boldsymbol{\lambda}_k^{(n)}$ and $\boldsymbol{\lambda}_{k+1}^{(n)}$, i.e.,

$$[(y_3 - y_2)(x_2 - x_1) - (x_3 - x_2)(y_2 - y_1)]$$
$$\cdot [(y_3 - y_2)(x_4 - x_2) - (x_3 - x_2)(y_4 - y_2)] < 0, \tag{27}$$

where, for simplicity, we have used the notations

$$\boldsymbol{\lambda}_{k-1}^{(n)} = [x_1, y_1]^\top, \quad \boldsymbol{\lambda}_k^{(n)} = [x_2, y_2]^\top, \quad \boldsymbol{\lambda}_{k+1}^{(n)} = [x_3, y_3]^\top, \quad \boldsymbol{\lambda}_{k+2}^{(n)} = [x_4, y_4]^\top.$$

It will not work if the convex condition (27) is violated when one of the four consecutive control points is duplicate or when $\boldsymbol{\lambda}_{k-1}^{(n)}$ and $\boldsymbol{\lambda}_{k+2}^{(n)}$ sit on opposite sides of $\overline{\boldsymbol{\lambda}_k^{(n)}\,\boldsymbol{\lambda}_{k+1}^{(n)}}$. However, when (27) is indeed violated, there are other ways to ensure the continuation of our algorithm. One way is to generate the two new vertices on an edge by using the S-shaped biarc, as illustrated in Fig. 3(b). Observe that there is a new parameter here for the selection of the break point on $\overline{\boldsymbol{\lambda}_k^{(n)}\,\boldsymbol{\lambda}_{k+1}^{(n)}}$ (with a simple selection as the middle point of $\overline{\boldsymbol{\lambda}_k^{(n)}\,\boldsymbol{\lambda}_{k+1}^{(n)}}$). Another way is to apply the de Rham-Chaikin scheme in (1)–(2). The latter, combined with our new scheme, is an adaptive scheme. For simplicity, this new adaptive scheme is applied in the sequel for not-locally-convex initial data. See Fig. 12 for the basis handling of the adaptive scheme.

We end this section by pointing out the circle, as illustrated in Fig. 9, does not have to be tangent to the three sides. Its radius, denoted by r_k, could be changed to

$$\text{radius} = \kappa_k r_k, \quad \kappa_k > 0. \tag{28}$$

Without going into too many details, we only demonstrate it by an example in Fig. 11.

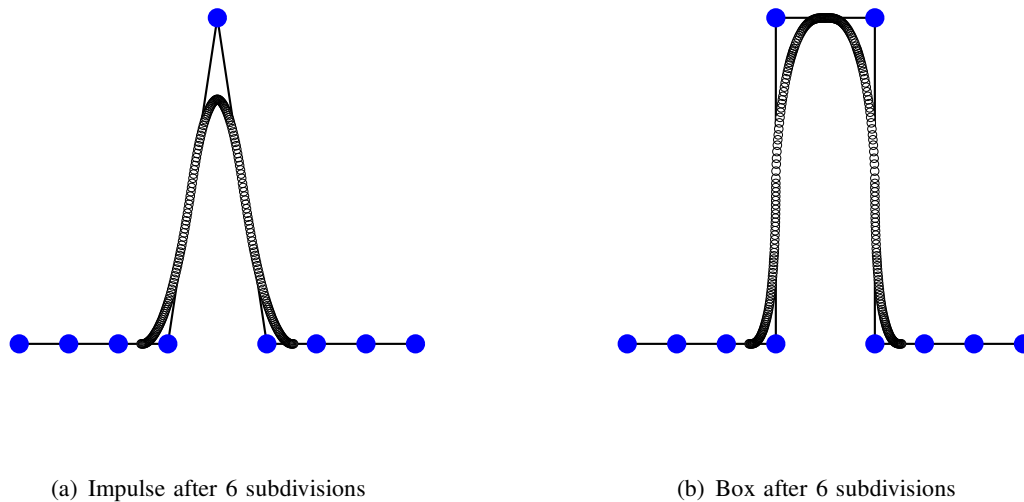(a) Impulse after 6 subdivisions   (b) Box after 6 subdivisions

Fig. 12.   Our adaptive subdivision scheme is applied to (a) an one-point-impulse; and (b) a 2-point-impulse, with results after 6 subdivisions ploted.
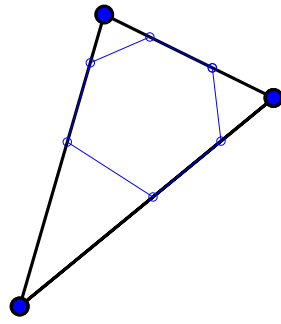
3.   Proof of Convergence

The convergence of both our new scheme and our new adaptive scheme is warranted by (de Boor [4]). Additional convergent study of both linear and nonlinear corner-cutting schemes can be found in, e.g., (Micchelli & Prautzsch [21], Micchelli & Prautzsch [22], Dyn, et al. [10], Gregory and Qu [16], Dyn [8]), and references therein. To have a better understanding of our new scheme for a strictly convex initial broken line, we sketch a brief demo in this section that our new nonlinear scheme does converge.

Theorem *1:* The new subdivision scheme described in Section 3 converges for any initial convex data set satisfying (27).
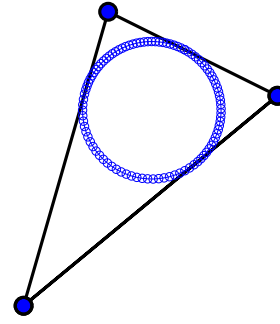
Proof. For convenience, we denote by A_1, A_2, B_2, and B_1 the vertices at $\boldsymbol{\lambda}_k^{(n)}$, $\boldsymbol{\lambda}_{2k}^{(n+1)}$, $\boldsymbol{\lambda}_{k+1}^{(n+1)}$, and $\boldsymbol{\lambda}_{k+1}^{(n)}$; $\alpha_{2k}^{(n+1)}$ the angle formed by the three new vertices $\boldsymbol{\lambda}_{2k-1}^{(n+1)}$, $\boldsymbol{\lambda}_{2k}^{(n+1)}$, and $\boldsymbol{\lambda}_{2k+1}^{(n+1)}$; $\alpha_{2k+1}^{(n+1)}$ the angle formed by $\boldsymbol{\lambda}_{2k}^{(n+1)}$, $\boldsymbol{\lambda}_{2k+1}^{(n+1)}$, and $\boldsymbol{\lambda}_{2k+2}^{(n+1)}$; and $r_k^{(n)}$ be the distance from $\mathbf{c}_k^{(n)}$ to the line formed by $\boldsymbol{\lambda}_k^{(n)}$ and $\boldsymbol{\lambda}_{k+1}^{(n)}$. Clearly, $r_k^{(n)}$ is the radius of the inscribed circle of the old four vertices. See Fig. 9.

Observe first that the two new vertices $\boldsymbol{\lambda}_{2k}^{(n+1)}$ and $\boldsymbol{\lambda}_{2k+1}^{(n+1)}$ are completely determined from the two old vertices $\boldsymbol{\lambda}_k^{(n)}$ and $\boldsymbol{\lambda}_{k+1}^{(n)}$, and the two angles $\alpha_k^{(n)}$ and $\alpha_{k+1}^{(n)}$. The latter of course also relies on $\boldsymbol{\lambda}_{k-1}^{(n)}$ and $\boldsymbol{\lambda}_{k+2}^{(n)}$.

Applications and Applied Mathematics: An International Journal (AAM), Vol. 7 [2012], Iss. 1, Art. 30

AAM: Intern. J., Vol. 7, Issue 1 (June 2012)   479
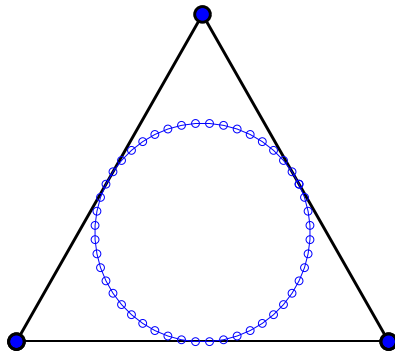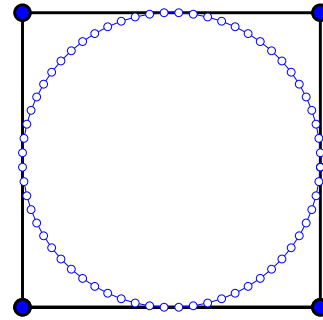
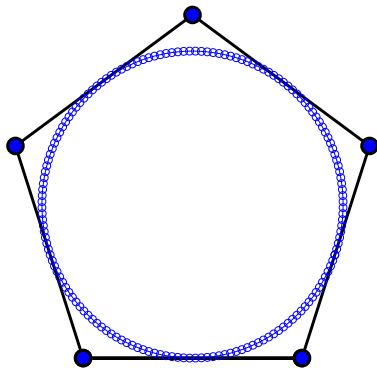(a) A scalene triangle after 1 subdivision

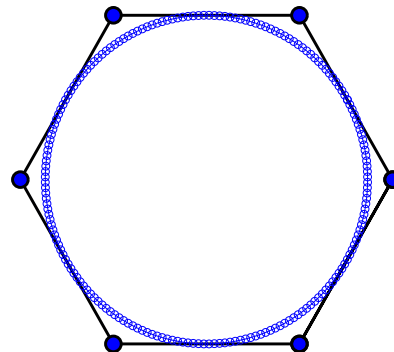(b) A scalene triangle after 5 subdivisions

(c) A equilateral triangle

(d) A square

(e) A regular pentagon

(f) A regular hexagon

Fig. 13.   Our subdivision scheme is applied to (a) a scalene triangle in Fig. 7 after 1 subdivision; (b) the same scalene triangle in Fig. 7 after 5 subdivisions; (c) an equilateral triangle; (d) a square; (e) a regular pentagon; and (f) a regular hexagon.
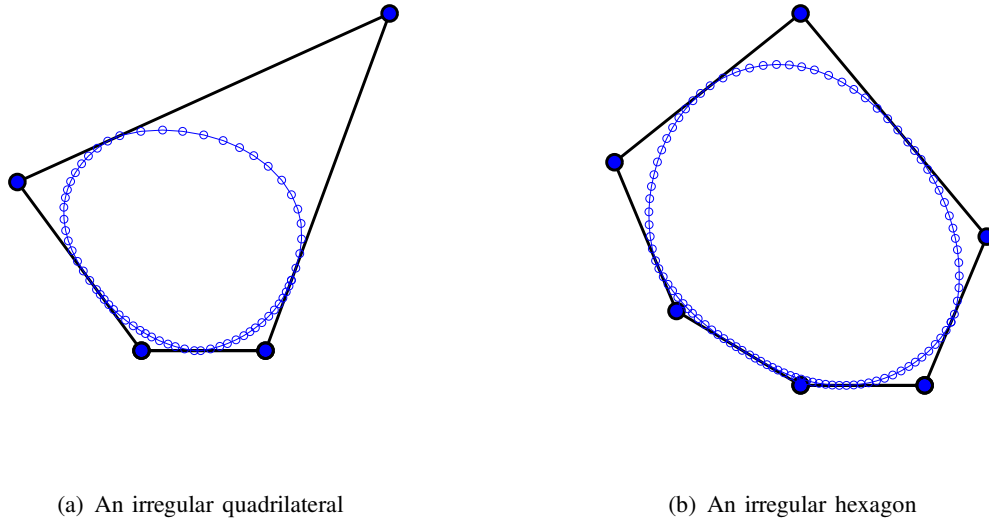
(a) An irregular quadrilateral   (b) An irregular hexagon

Fig. 14.   Our subdivision scheme is applied to (a) an irregular quadrilateral, and (c) an irregular hexagon.

It follows from

$$A_1B_1 = r_k^{(n)}\left(\cot\frac{\alpha_k^{(n)}}{2} + \cot\frac{\alpha_{k+1}^{(n)}}{2}\right), \quad A_2B_2 = r_k^{(n)}\left(\tan\frac{\pi - \alpha_k^{(n)}}{4} + \tan\frac{\pi - \alpha_{k+1}^{(n)}}{4}\right),$$

$$A_1A_2 = r_k^{(n)}\frac{\tan\dfrac{\pi - \alpha_k^{(n)}}{4}}{\cos\dfrac{\pi - \alpha_k^{(n)}}{2}}, \quad B_1B_2 = r_k^{(n)}\frac{\tan\dfrac{\pi - \alpha_{k+1}^{(n)}}{4}}{\cos\dfrac{\pi - \alpha_{k+1}^{(n)}}{2}},$$

that $\omega_{k,1}^{(n)}$ and $\omega_{k,2}^{(n)}$ in (25)-(26) are given by

$$\omega_{k,1}^{(n)} = \frac{\tan\dfrac{\pi - \alpha_k^{(n)}}{4}}{\cos\dfrac{\pi - \alpha_k^{(n)}}{2}\left(\tan\dfrac{\pi - \alpha_k^{(n)}}{2} + \tan\dfrac{\pi - \alpha_{k+1}^{(n)}}{2}\right)}, \tag{29}$$

$$\omega_{k,2}^{(n)} = \frac{\tan\dfrac{\pi - \alpha_{k+1}^{(n)}}{4}}{\cos\dfrac{\pi - \alpha_{k+1}^{(n)}}{2}\left(\tan\dfrac{\pi - \alpha_k^{(n)}}{2} + \tan\dfrac{\pi - \alpha_{k+1}^{(n)}}{2}\right)}. \tag{30}$$

Simple calculation leads to

$$1 - \omega_{k,1}^{(n)} - \omega_{k,2}^{(n)} = \frac{\tan\dfrac{\pi - \alpha_k^{(n)}}{4} + \tan\dfrac{\pi - \alpha_{k+1}^{(n)}}{4}}{\tan\dfrac{\pi - \alpha_k^{(n)}}{2} + \tan\dfrac{\pi - \alpha_{k+1}^{(n)}}{2}}. \tag{31}$$

Applications and Applied Mathematics: An International Journal (AAM), Vol. 7 [2012], Iss. 1, Art. 30

AAM: Intern. J., Vol. 7, Issue 1 (June 2012)   481

(a) Initial and 1 subdivision

(b) After 6 subdivisions

(c) Initial and 6 subdivisions
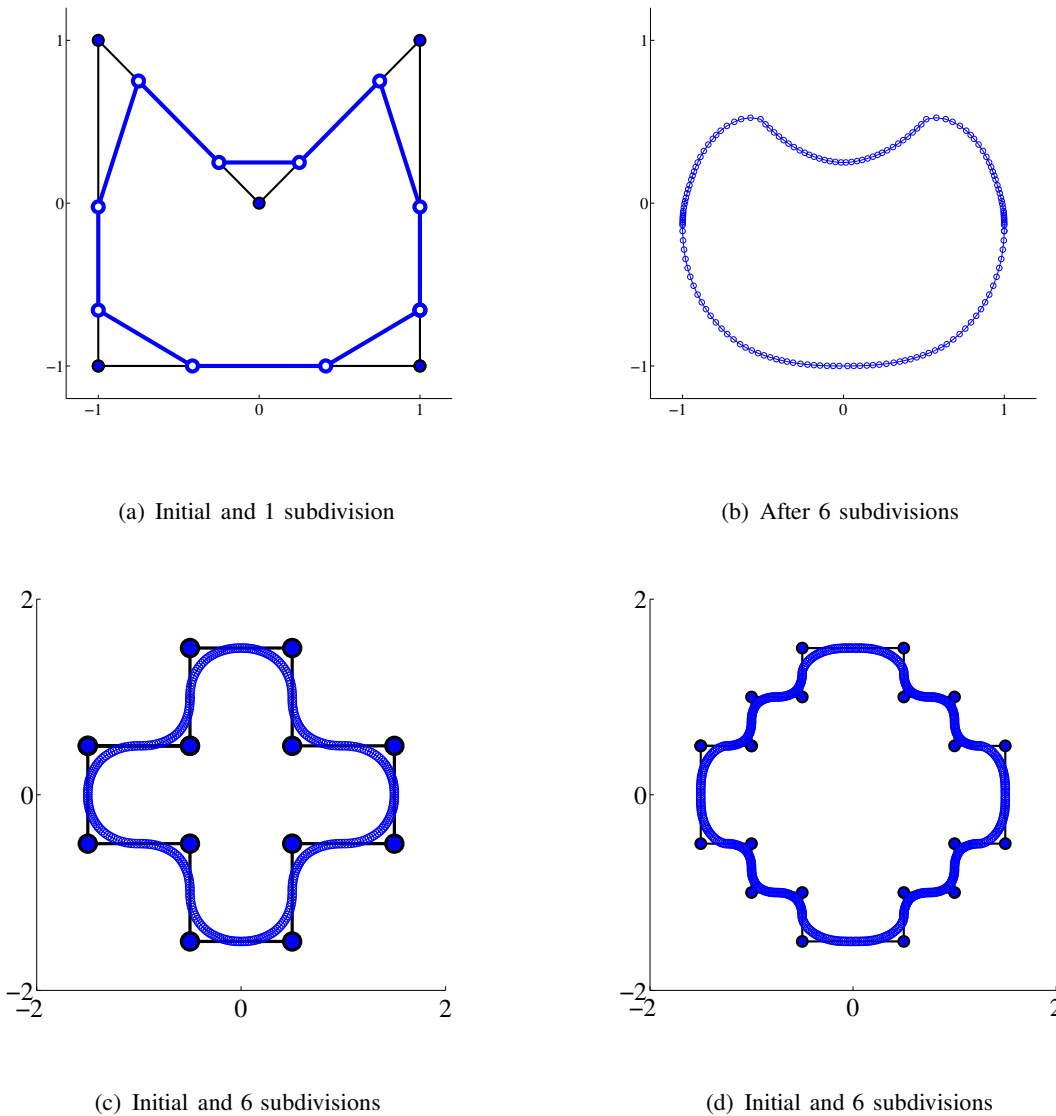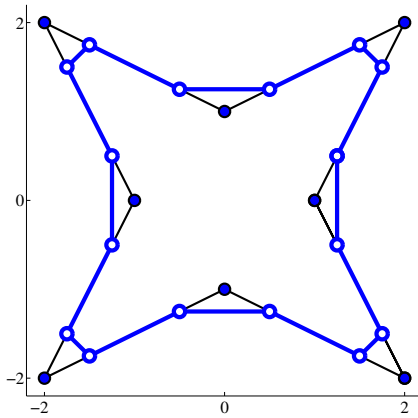
(d) Initial and 6 subdivisions

Fig. 15.   Our adaptive subdivision scheme is applied to (a) a non-convex pentagon: initial and after 1 subdivision; (b) the non-convex pentagon after 6 subdivisions; (c) a cross-shaped polygon: initial and after 6 subdivisions; and (d) another cross-shaped polygon: initial and after 6 subdivisions.

Rewrite (25)-(26) into a matrix form

$$\begin{bmatrix} \boldsymbol{\lambda}_{2k}^{(n+1)} & \boldsymbol{\lambda}_{2k+1}^{(n+1)} \end{bmatrix} = \begin{bmatrix} \boldsymbol{\lambda}_k^{(n)} & \boldsymbol{\lambda}_{k+1}^{(n)} \end{bmatrix} \left(M_k^{(n)} \right)^\top, \tag{32}$$

$$M_k^{(n)} = \begin{bmatrix} 1 - \omega_{k,1}^{(n)} & \omega_{k,1}^{(n)} \\ \omega_{k,2}^{(n)} & 1 - \omega_{k,2}^{(n)} \end{bmatrix}. \tag{33}$$
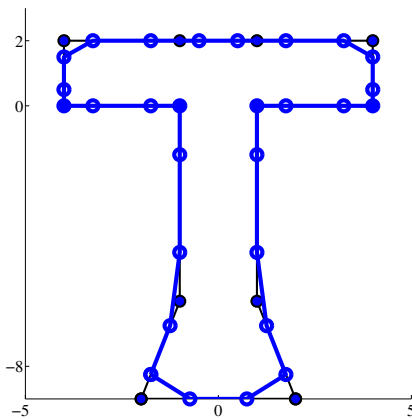
The row-stochastic matrix $M_k^{(n)}$ in (33) has eigenvalues 1 and $1 - \omega_{k,1}^{(n)} - \omega_{k,2}^{(n)}$, with corresponding eigenvectors $\begin{bmatrix} 1 & 1 \end{bmatrix}^\top$ and $\begin{bmatrix} \omega_{k,1}^{(n)} & -\omega_{k,2}^{(n)} \end{bmatrix}^\top$. The corresponding eigenvectors of $\left(M_k^{(n)} \right)^\top$ are $\begin{bmatrix} \omega_{k,2}^{(n)} & \omega_{k,1}^{(n)} \end{bmatrix}^\top$ and $\begin{bmatrix} 1 & -1 \end{bmatrix}^\top$. Hence, a product of a sequence of matrices as in (33) for
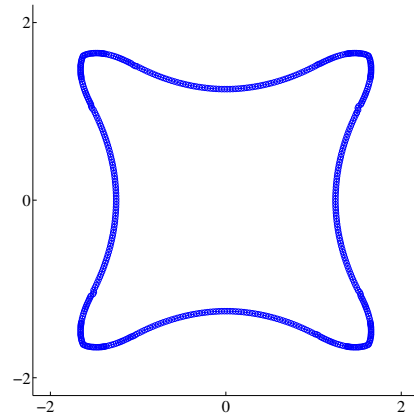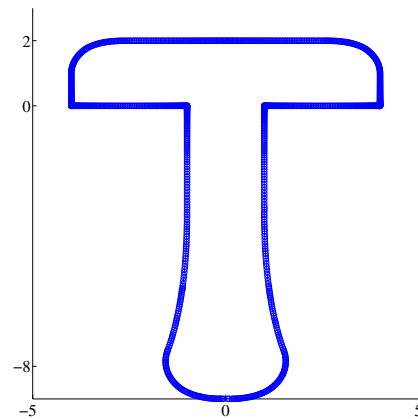
(a) Initial and 1 subdivision   (b) After 6 subdivisions

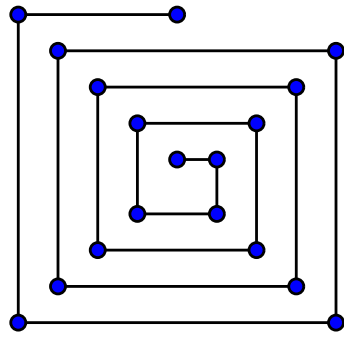(c) Initial and after 1 subdivision   (d) After 6 subdivisions

Fig. 16. Our adaptive subdivision scheme is applied to (a) a non-convex 4-corner polygon: initial and after 1 subdivision; (b) the non-convex 4-corner polygon after 6 subdivisions; (c) a T-shaped polygon with 4 repeated vertices at $(-4, 0)$, $(-1, 0)$, $(1, 0)$, and $(4, 0)$: initial and after 1 subdivision; and (d) the T-shaped polygon after 6 subdivisions. The four (4) sharp corners in (d) were caused by the repetition of the four vertices in the initial data.

consecutive k's has eigenvalues 1 and the product of $\left(1 - \omega_{k,1}^{(n)} - \omega_{k,2}^{(n)}\right)$'s. This is due to the following two facts: (1) a product of two row-stochastic matrices is also row-stochastic, and (2) if two same size matrices A and B have a common eigenvector $\mathbf{x}$ with eigenvalues λ_A and λ_B then AB has eigenvalue $\lambda_A \lambda_B$ with eigenvector $\mathbf{x}$ too.
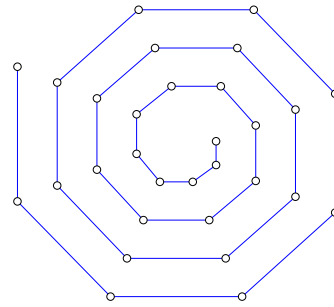
The convergence then follows from the fact that, from (31),

$$0 < 1 - \omega_{k,1}^{(n)} - \omega_{k,2}^{(n)} < \frac{1}{2}, \quad \alpha_k^{(n)}, \alpha_{k+1}^{(n)} \in (0, \pi).$$
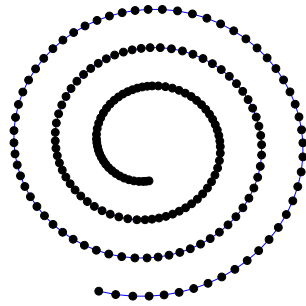
This completes the proof of Theorem 1. ∎

Applications and Applied Mathematics: An International Journal (AAM), Vol. 7 [2012], Iss. 1, Art. 30

AAM: Intern. J., Vol. 7, Issue 1 (June 2012)   483
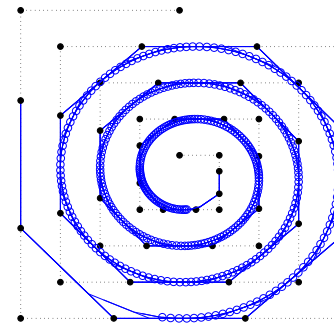
(a) Initial data   (b) After 1 subdivision

(c) After 4 subdivisions   (d) Initial and after 1 and 5 subdivisions

Fig. 17.   Our subdivision scheme is applied to (a) an initial spiral data set, with results after one and four subdivisions given in (b) and (c). Initial data and both results after 1 and 5 subdivisions are illustrated in (d).

4.   Implementation by Examples

We implement our new subdivision scheme described in §3 by a variety of examples.

First, to ensure our new subdivision scheme is circular invariant, we apply the scheme to an equilateral triangle and a square, a regular pentagon, and a regular hexagon, as shown in Fig. 13. Here, vertices after the 2nd-level subdivision are also plotted.

Next, we apply our scheme to an irregular quadrilateral and an irregular hexagon, as shown in Fig. 14. Fig. 15 and Fig. 16 show the adaptiveness of the scheme when the convex property is violated, where our adaptive scheme is applied to a variety of polygons, namely, a non-convex pentagon; two cross-shaped polygons; non-convex 4-corner polygon; and a T-shaped polygon with 4 repeated vertices (at which the limiting curve is interpolatory and has sharp turns). Finally, Fig. 17 shows when our scheme is applied to a spiral-shaped data set.

5. Conclusion

A new subdivision scheme for 2D planar curve design is established. The scheme is nonlinear, circular-invariant, and derived from a special C-shaped biarc circular spline structure. It can be easily applied to any 2D planar set of vertices that is convex. It is adaptive if the convex property of a set of four consecutive vertices is violated. We will further investigate in the near future the similar scheme for 3D curve design and 3D surface design (Lian & Yang [19], Yang & Lian [34]). The scheme for the latter should be sphere-invariant.

Appendix A: Why Linear Schemes Are Not Circular-Invariant

It can be proved directly that any linear scheme is not circular-invariant. To verify this fact, we need to look into the closed forms of limiting curves.

Fix an initial polygon as a square for the moment, for example, with four vertices at

$$\boldsymbol{\lambda}_0^{(0)} = [-1, -1]^\top, \quad \boldsymbol{\lambda}_1^{(0)} = [1, -1]^\top, \tag{34}$$

$$\boldsymbol{\lambda}_2^{(0)} = [1, 1]^\top, \quad \boldsymbol{\lambda}_3^{(0)} = [-1, 1]^\top. \tag{35}$$

It has been shown in the wavelet literature that, with (34)–(35) as vertices of an initial polygon, the limiting curves of the four schemes can be explicitly written as a linear combinations of *refinable* functions (cf., e.g., Micchelli & Prautzsch [21], Finkelstein and Salesin [15]). More precisely, the limiting curves in their parametric forms of the de Rham-Chaikin scheme in (1)–(2), the DLG scheme in (3)–(4), the N_6-induced binary scheme in (5)–(6), and the N_5-induced ternary scheme in (7)–(9), are

$$\begin{bmatrix} x_{\mathrm{RC}}(t) \\ y_{\mathrm{RC}}(t) \end{bmatrix} = \sum_{k=0}^{5} \boldsymbol{\lambda}_k^{(0)} N_3(t-k), \quad 2 \le t \le 6; \tag{36}$$

$$\begin{bmatrix} x_{\mathrm{DLG}}(t) \\ y_{\mathrm{GLG}}(t) \end{bmatrix} = \sum_{k=-2}^{6} \boldsymbol{\lambda}_k^{(0)} \phi_{\mathrm{DLG}}(t-k), \quad 3 \le t \le 7; \tag{37}$$

$$\begin{bmatrix} x_{\mathrm{N}_6}(t) \\ y_{\mathrm{N}_6}(t) \end{bmatrix} = \sum_{k=-2}^{6} \boldsymbol{\lambda}_k^{(0)} N_6(t-k), \quad 3 \le t \le 7; \tag{38}$$

$$\begin{bmatrix} x_{\mathrm{N}_5}(t) \\ y_{\mathrm{N}_5}(t) \end{bmatrix} = \sum_{k=-1}^{6} \boldsymbol{\lambda}_k^{(0)} N_5(t-k), \quad 3 \le t \le 7. \tag{39}$$

Here, again, N_3, N_6, and N_5 are the 3rd-, 6th- and 5th-order cardinal B-splines, which are refinable and shown in Fig. 8 (a), Fig. 8 (c), and Fig. 8 (d); ϕ_{DLG} is the refinable function, shown in Fig. 8 (b); and the additional necessary vertices are defined periodically, i.e., $\boldsymbol{\lambda}_{-2}^{(0)} = \boldsymbol{\lambda}_2^{(0)}$, $\boldsymbol{\lambda}_{-1}^{(0)} = \boldsymbol{\lambda}_3^{(0)}$; $\boldsymbol{\lambda}_4^{(0)} = \boldsymbol{\lambda}_0^{(0)}$, $\boldsymbol{\lambda}_5^{(0)} = \boldsymbol{\lambda}_1^{(0)}$, $\boldsymbol{\lambda}_6^{(0)} = \boldsymbol{\lambda}_2^{(0)}$.

It is then straightforward to verify that each of the two limiting curves in (36)–(37) is not a

Applications and Applied Mathematics: An International Journal (AAM), Vol. 7 [2012], Iss. 1, Art. 30

AAM: Intern. J., Vol. 7, Issue 1 (June 2012)   485

circle, e.g., due to their interpolatory property,

$$[x_{RC}(t)]^2 + [y_{RC}(t)]^2 \not\equiv 1, \quad 2 \leq t \leq 6; \tag{40}$$
$$[x_{DLG}(t)]^2 + [y_{DLG}(t)]^2 \not\equiv 2, \quad 3 \leq t \leq 7.$$

To be certain that the two other limiting curves in (38)–(39) are not circles, namely,

$$[x_{N_6}(t)]^2 + [y_{N_6}(t)]^2 \not\equiv c_1, \quad 3 \leq t \leq 7, \tag{41}$$
$$[x_{N_5}(t)]^2 + [y_{N_5}(t)]^2 \not\equiv c_2, \quad 3 \leq t \leq 7,$$

for some positive constants c_1 and c_2, we provide the following simple proof.

Theorem *2:* With four vertices of a square given by (35) as the initial vertices, there is no convergent linear subdivision scheme that generates a limiting curve as a circle.

Proof. First, a typical linear a-ary subdivision scheme has the form

$$\boldsymbol{\lambda}_{ak+j}^{(n+1)} = \sum_{\ell \in \mathbb{Z}} p_{a\ell+j} \boldsymbol{\lambda}_{k-\ell}^{(n)}, \quad j = 0, \ldots, a-1; \; k \in \mathbb{Z}. \tag{42}$$

Without loss of generality, we assume that the finite sequence $\{p_k\}_{k=0}^M$ satisfies $p_0 p_M \neq 0$. Second, corresponding to the finite sequence $\{p_k\}_{k=0}^M$ in (42), there is a refinable function ϕ satisfying

$$\phi(t) = \sum_{k \in \mathbb{Z}} p_k \phi(at - k), \quad t \in \mathbb{R}, \tag{43}$$

which has $\operatorname{supp} \phi = \left[0, \dfrac{M}{a-1}\right]$. By defining additional necessary vertices periodically, e.g.,

$$\boldsymbol{\lambda}_{k+4\ell}^{(0)} = \boldsymbol{\lambda}_k^{(0)}, \quad k = 0, \ldots, 3; \; \ell \in \mathbb{Z},$$

the limiting curve can be expressed as

$$\begin{bmatrix} x(t) \\ y(t) \end{bmatrix} = \sum_{k=L_1}^{L_2} \boldsymbol{\lambda}_k^{(0)} \phi(t-k), \quad n_1 \leq t \leq n_2. \tag{44}$$

It then follows from (44) that

$$\begin{bmatrix} x(t) \\ y(t) \end{bmatrix} = \boldsymbol{\lambda}_{L_1}^{(0)} \phi(t-L_1), \quad n_1 \leq t \leq n_1 + 1,$$

so that

$$[x(t)]^2 + [y(t)]^2 = 2\left[\phi(t-L_1)\right]^2, \quad n_1 \leq t \leq n_1 + 1.$$

Hence, if the limiting curve in (44) is a full circle, i.e., $[x(t)]^2 + [y(t)]^2 = c$ for some positive constant c, then $\phi(t-L_1)$ is constant on $[n_1, n_1+1)$. Similar derivation by using (44) leads to the conclusion that $\phi(t)$ is constant for all $t \in [n_1, n_2]$, which contradicts the fact that (44) represents a full circle. This completes the proof of Theorem 2. ∎

Appendix B: Proof of Identity (15)

Let O in Fig. 2 be the origin of the coordinate system and introduce

$$W_1(t) = -aB_{0,2}(t) + aB_{2,2}(t),$$

$$W_2(t) = \frac{ah}{\sqrt{a^2 + h^2}} B_{1,2}(t),$$

$$W(t) = B_{0,2}(t) + \frac{a}{\sqrt{a^2 + h^2}} B_{1,2}(t) + B_{2,2}(t).$$

Then, the equation of the circle is

$$\left(\frac{W_1(t)}{W(t)}\right)^2 + \left(\frac{W_2(t)}{W(t)} + \frac{a^2}{h}\right)^2 = \frac{a^2(a^2 + h^2)}{b^2},$$

which leads to

$$W_1(t)^2 + W_2(t)^2 + \frac{2a^2}{h}W_2(t)W(t) = a^2 W(t)^2. \tag{45}$$

Hence,

$$\begin{aligned}
\|\boldsymbol{p}(t) - \boldsymbol{\lambda}_0\| W(t)^2 &= (W_1(t) + aW(t))^2 + W_2(t)^2 \\
&= W_1(t)^2 + 2aW_1(t)W(t) + a^2 W(t)^2 + W_2(t)^2 \\
&= 2a^2 W(t)^2 - \frac{2a^2}{h}W_2(t)W(t) + 2aW_1(t)W(t) \\
&= \frac{2a}{h}W(t)\left[ahW(t) - aW(t) + hW_1(t)\right] \\
&= 4a^2 W(t)\, t^2,
\end{aligned} \tag{46}$$

where (45) was used in the third equality. Similarly,

$$\begin{aligned}
\|\boldsymbol{p}(t) - \boldsymbol{\lambda}_2\| W(t)^2 &= \frac{2a}{h}W(t)\left[ahW(t) - aW(t) - hW_1(t)\right] \\
&= 4a^2 W(t)\,(1 - t)^2.
\end{aligned} \tag{47}$$

It follows from both (46) and (47) that

$$\|\boldsymbol{p}(t) - \boldsymbol{\lambda}_0\| = \frac{2a}{\sqrt{W(t)}}t, \qquad \|\boldsymbol{p}(t) - \boldsymbol{\lambda}_2\| = \frac{2a}{\sqrt{W(t)}}(1 - t). \tag{48}$$

Due to the fact that $W(1 - t) = W(t)$, it is easy to see that

$$\|\boldsymbol{p}(t) - \boldsymbol{\lambda}_0\| + \|\boldsymbol{p}(t) - \boldsymbol{\lambda}_2\| = \frac{2a}{\sqrt{W(t)}}. \tag{49}$$

Therefore, (15) follows from both (48) and (49). This completes the proof of (15). ∎

REFERENCES

[1] U.H. Augsdörfer, N.A. Dodgson, and M.A. Sabin, "Variations on the four-point subdivision scheme," *Computer-Aided Geometric Design* **27** (2010), 78–95.

Applications and Applied Mathematics: An International Journal (AAM), Vol. 7 [2012], Iss. 1, Art. 30

AAM: Intern. J., Vol. 7, Issue 1 (June 2012) 487

[2] C. Beccari, G. Casciola, L. Romani, "A non-stationary uniform tension controlled interpolating 4-point scheme reproducing conics," *Computer-Aided Geometric Design* **24** (2007), 1–9.

[3] K.M. Bolton, "Biarc curves," *Computer-Aided Design* **7**(2) (1975), 89–92.

[4] C. de Boor, "Cutting comers always works," *Computer-Aided Geometric Design* **4** (1987), 125–131.

[5] G.M. Chaikin, "An algorithm for high speed curve generation," *Computer Vision, Graphics and Image Processing* **3** (1974), 346–349.

[6] P. Chalmovianský and B. Jüttler, "A non-linear circle-preserving subdivision scheme," *Adv. Compu. Math.* **27** (2007), 375–400.

[7] C.K. Chui, "*Multivariate Splines*," SIAM, Philadelphia, PA, 1988.

[8] N. Dyn, "Analysis of convergence and smoothness by the formalism of Laurent polynomials," in: *Tutorials on Multiresolution in Geometric Modeling*, A. Iske, E. Quak and M.S. Floater (eds.), Springer-Verlag, Heidelberg, 2002, 51–68.

[9] N. Dyn, D. Levin, and J. Gregory, "A 4-point interpolatory subdivision scheme for curve design," *Computer Aided Geometric Design* **4** (1987), 257-268.

[10] N. Dyn, J. A. Gregory, and D. Levin, "Analysis of uniform binary subdivision schemes for curve design," *Const. Approx.* **7** (1991), 127–147.

[11] G. Farin, *NURB Curves and Surfaces*, 2nd ed., AK Peters, Boston 1999.

[12] G. Farin, *Curves and Surfaces for Computer Aided Geometric Design*, 5th ed., Morgan Kaufmann, 2001.

[13] G. Farin, "Rational quadratic circles are parameterized by chord length," *Computer-Aided Geometric Design* **23** (2006), 722–724.

[14] G. Farin, "Geometric Hermite interpolation with circular precision," *Computer-Aided Design* **40** (2008), 476–479.

[15] A. Finkelstein and D. Salesin, "Multiresolution curves," in: SIGGRAPH'94: *Proceedings of the 21st Annual Conference on Computer Graphics and Interactive Techniques*, ACM, New York, NY, 1994, 261–268.

[16] J. A. Gregory and R. Qu, "Nonuniform corner cutting," *Computer-Aided Geometric Design* **13** (1996), 763–772.

[17] J. Hoschek, "Circular splines," *Computer-Aided Design* **24**(11) (1992), 611–618.

[18] J.-A. Lian, Y. Wang, and Y. Yang, "Circular nonlinear subdivision schemes for curve design," *Applications and Applied Math.* **4** (2009), 1–12.

[19] J.-A. Lian and Y. Yang, "A new cross subdivision scheme for surface design," *Journal of Mathematical Analysis and Applications* **354** (2011), 244–257.

[20] D. Meek and D. Walton, "Approximation of discrete data by G^1 arc splines," *Computer-Aided Design* **24**(6) (1992), 301–306.

[21] C.A. Micchelli and H. Prautzsch, "Refinement and subdivision for spaces of integer translates of a compactly supported function," in: *Numerical Analysis 1987 (Dundee, 1987)*, D.F. Griffiths and G.A. Watson (eds.), Pitman Res. Notes Math Ser., 170, Longman Sci. Tech., Halow, 1988, 192–222.

[22] C.A. Micchelli and H. Prautzsch, "Uniform refinement of curves," *Linear Algebra and Its Applications* **114/115** (1989), 841–870.

[23] D.N. Moreton and D.B. Parkinson, "The application of a biarc technique in CNC machining," *IEE Computer Aided Engineering Journal* **8**(2) (1991), 54–60.

[24] A. Nasri and G. Farin, "A subdivision algorithm for generating rational curves," *J. Graphics Tools* **6** (2001), 35–47.

[25] A. Nasri, C. W. A. M. van Overveld, and B. Wyvill, "A recursive subdivision algorithm for piecewise circular spline," *Computer Graphics Forum* **20** (2001), 35–45.

[26] C.J. Ong,Y.. Wong, H.T. Loh, and X.G. Hong, "An optimization approach for biarc curve-fitting of *B*-spline curves," *Computer Aided Design* **28**(12) (1996), 951–959.

[27] L. Piegl, "The sphere as a rational Bézier surface," *Computer Aided Geometric Design* **3** (1986), 45–52.

[28] L. Piegl and W. Tiller, *The NURBS Book*, 2nd ed., Springer-Verlag, Berlin, 1997.

[29] L. Piegl and W. Tiller, "Biarc approximation of NURBS curves," *Computer Aided Design* **34**(11) (2002), 807–814.

[30] L. Romani, "A circle-preserving C^2 Hermite interpolatory subdivision scheme with tension control," *Computer Aided Geometric Design* **27** (2010), 36–47.

[31] J. Schönherr, "Smooth biarc curves," *Computer Aided Design* **25**(6) (1993), 365–370.

[32] Y.S. Wong, H.T. Loh, and K.S. Neo, Computer-aided design (CAD) for the translation of geometric data to numerical control (NC) programs for manufacturing systems, Chapter 2 of Book in: "*Computer-Aided Design, Engineering, and Manufacturing Systems Techniques and Applications, Volume III, Operational Methods in Computer-Aided Design*," C. T. Leondes ed., CRC Press, Boca Raton, Florida, 2001, 2.1–2.37.

[33] X. Yang and Z.C. Chen, "A practicable approach to G^1 biarc approximations for making accurate, smooth and non-gouged profile features in CNC contouring," *Computer Aided Design* **38**(11) (2006),1205–1213.

[34] Y. Yang and J.-A. Lian, "Making 3D object surfaces smoother: Two new interpolating subdivision schemes," *IEEE Computing in Science & Engineering* **12** (2010), 44–50.